nature communications

Article

https://doi.org/10.1038/s41467-024-51607-z

TPE-embedded butterfly bis-crown ether with controllable conformation and supramolecular chiroptical property

Received: 25 March 2024

Accepted: 13 August 2024

Published online: 21 August 2024

Check for updates

Xueqi Tian[1,2,4], Minzan Zuo[1,4], Yuhong Shen[3], Ni Mao[1], Kaiya Wang[1], Yanshan Sheng[1], Krishnasamy Velmurugan[1], Jianmin Jiao[2] & Xiao-Yu Hu[1,2]

Understanding how subtle structural differences between macrocyclic conformational isomers impact their properties and separation has garnered increasing attention in the field of supramolecular synthetic chemistry. In this work, a series of tetraphenylene (TPE)-embedded butterfly bis-crown ether macrocycles (**BCE[n]**, $n = 4–7$), comprising two crown ether side rings and a TPE core, are synthesized through intramolecular McMurry coupling. Unexpectedly, the presence of flexible oligoethylene chains with varying lengths are found to influence molecular conformation via multiple intramolecular interactions, resulting in the formation of two stabilized conformers with specific semi-rigid symmetric/asymmetric structures (***sym*-BCE[n]** and ***asym*-BCE[n]**, $n = 5, 6$). Moreover, it is noteworthy that neither symmetric nor asymmetric conformers are present in the more rigid **BCE[4]** or the more flexible **BCE[7]**. Interestingly, these conformers display distinct fluorescence properties and host-guest binding abilities, and only ***sym*-BCE[5]** can serve as a host for chiral polymer binding, resulting in the formation of chiral supramolecular assemblies through host-guest interaction induced chirality. Moreover, both circular dichroism and circularly polarized luminescence signals of the obtained assemblies can be switched off by the addition of sodium ion, suggesting potential applications in the field of dynamic chiral materials.

Tetraphenylethylene (TPE) represents one of the most prevalent aggregation-induced emission (AIE)-active moieties, making it an ideal fluorescent building block for integration into macrocycles[1–7]. It is noteworthy that a TPE derivative theoretically possesses a diverse range of conformations, which are determined by the varying dihedral angles within the TPE core. Manipulating these conformational changes can lead to compounds with distinct photophysical properties[8–13]. By restricting the dihedral angles in the AIE compounds, these molecules with diverse conformations hold great potential for precise modulation of material functionalities[14–17]. Moreover, the TPE group exhibits either clockwise or anticlockwise rotational patterns in its propeller-like *P* or *M* configurations, respectively, by restricting the intramolecular flipping of phenyl rings. For example, the *P* or *M* configurations of TPE can also be constrained through the introduction of a rigid cyclic structure, offering the possibility for construction of chiral materials[18–21]. So far, achieving distinct conformations for TPE compounds remains a formidable challenge.

Herein, we report the synthesis of a series of TPE-based bis-crown ethers (**BCE[n]**, $n = 4–7$) through intramolecular McMurry coupling interaction. In order to achieve AIE-active macrocycles with distinct conformations in both solution and solid state, chains with appropriate length were introduced to connect the phenyl-substituents,

[1]College of Materials Science and Technology, Nanjing University of Aeronautics and Astronautics, Nanjing, China. [2]College of Chemistry and Chemical Engineering, Jiangxi Normal University, Nanchang, China. [3]School of Chemistry and Chemical Engineering, Nanjing University, Nanjing, China. [4]These authors contributed equally: Xueqi Tian, Minzan Zuo. e-mail: huxy@nuaa.edu.cn

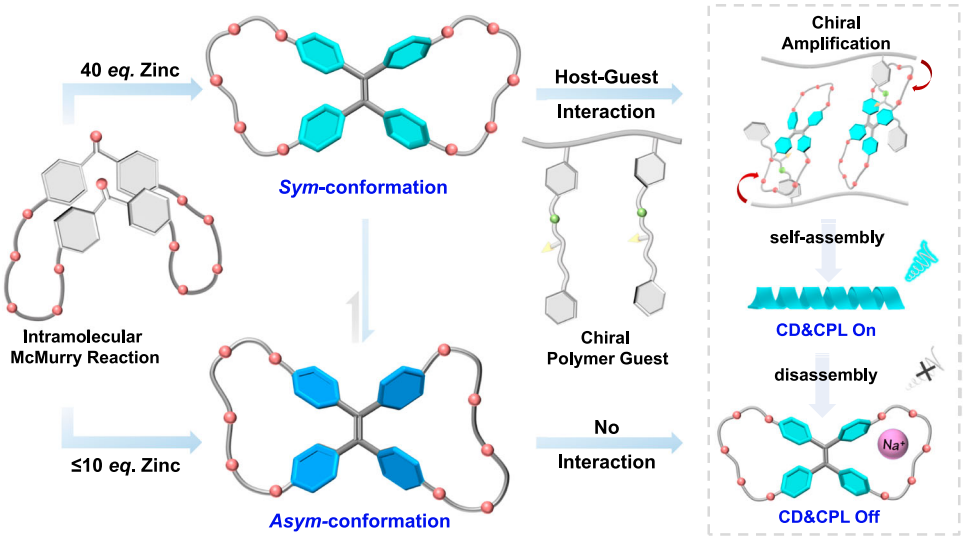

Fig. 1 | Cartoon representations for construction of BCE[5] isomers and chiroptical application. Schematic illustration of the two conformations of bis-crown ether macrocycles and the guest-modulated chiroptical signal in the assembled system.

thereby restricting the dihedral angles of TPE core. The TPE unit was cyclized through flexible ethylene glycol chains, and it was observed that varying chain lengths resulted in different degrees of distortion in the TPE core due to intramolecular tension. Surprisingly, both **BCE**[5] and **BCE**[6] exhibit two conformations, namely ***sym*-BCE[n]** and ***asym*-BCE[n]** ($n = 5, 6$), respectively. Moreover, it is noteworthy that neither symmetric nor asymmetric conformer is present in the more rigid **BCE**[4] or the more flexible **BCE**[7]. Furthermore, variations in cavity size and shape result in diverse fluorescence and binding properties among different conformers. It is worth noting that only ***sym*-BCE**[5] can act as a host for chiral polymer guest binding, thereby enabling the generation of chiral materials with controllable handedness through supramolecular chiral amplification induced by host-guest interaction (Fig. 1).

Results

Synthesis and structural characterization

TPE-cored butterfly-shaped macrocycles were synthesized by embedding TPE units into crown ether through a facile three-step process (Fig. 2). Our methodology distinguishes itself from previous reports on crown ether-functionalized TPE-based macrocycles obtained through direct intermolecular cyclization[22–24], as it is challenging to achieve high yields of smaller-sized crown ether ring-functionalized TPE-macrocycles due to the strain resulting from intramolecular cyclization.

BCE[n] ($n = 4–7$) with identical skeletal structures but varying lengths of crown ether chains were synthesized, and the synthesis route as well as the detailed procedures are elaborated in Supplementary Figs. 14, 27. Taking **BCE**[5] as a representative example, we first obtained the cyclic diketone by reacting two dihydroxybenzophenone molecules with two equivalents of tetraethylene glycol ditosylate in a highly concentrated reaction solution (Supplementary Figs. 1–13). With the diketone in hand, the target macrocycle **BCE**[5] could be efficiently obtained via an intramolecular McMurry reaction in the final coupling step. As expected, three additional **BCE[n]** ($n = 4, 6, 7$) were also successfully prepared using this convenient methodology with moderate yields (Supplementary Figs. 14, 27). The obtained **BCE[n]** were fully characterized by ^{1}H NMR, ^{13}C NMR, HR-ESI-MS, and single crystal analyses to validate their structural integrity (Supplementary Figs. 15–26, 28–33).

The reaction of the diketone compound with zinc powder (5 equiv.) and $TiCl_4$ (2.5 equiv.) resulted in the formation of **BCE**[5] product, which was obtained with a moderate yield (38%). This product exhibited blue color in solid state under UV-irradiation. To further optimize the yield, we explored the feasibility of increasing the quantity of zinc powder by varying its ratio from 5 to 40 equivalents. The ^{1}H NMR spectra revealed slight variations in the products obtained under different conditions of zinc powder equivalents (Supplementary Fig. 40). In Fig. 3a and Supplementary Fig. 15, it is evident that reducing the amount of zinc powder used in the reaction resulted in the observation of two distinct peaks at 6.68 and 6.91 ppm for the C–H protons of the aromatic protons in the product, as observed in $CDCl_3$. However, when increasing the amount of zinc powder to 20 equiv. and 30 equiv., a broadening peak resembling a mixture was observed, indicating the gradual formation of side-products (Supplementary Fig. 40). By employing 40 equiv. of zinc powder, another pure product was successfully obtained as confirmed by the ^{1}H NMR spectra (Supplementary Fig. 18). Interestingly, this product exhibits a distinct green color in its solid state under UV-irradiation. Additionally, its ^{1}H NMR spectrum shows slight differences compared to the previously mentioned product. Specifically, the resonance peaks at 6.82 and 6.88 ppm show increased proximity to each other, and its ($-OCH_2$) signal corresponding to the ether chains displays a slightly downfield chemical shift (Fig. 3a). Notably, there is also noticeable disparity between the chemical shifts of these two products around 130–140 ppm on the ^{13}C NMR spectra (Supplementary Figs. 16, 20). Furthermore, mass spectrometry analysis confirmed that both products possessed identical molecular weight consistent with our target molecule, suggesting the formation of two conformers (Supplementary Figs. 17, 20). By varying the amount of zinc powder from 5 to 40 equiv., column chromatography demonstrated controllable production of these two products with different yields (Fig. 3b). The yield of the blue conformer gradually decreased as more zinc powder is used, while conversely, the yield of the green conformer gradually increased.

The single crystals of both products were obtained through slow vapor diffusion of *n*-hexane into chloroform solution containing the macrocycles. The crystal structures confirm that the macrocycles consist of a TPE core and two crown ether rings positioned on either side (Supplementary Figs. 44, 45). Similar to other TPE derivatives, the four phenyl rings are not coplanar with the central C = C double bond, resulting in a characteristic propeller-like structure. The solid state structure of the product obtained with 10 equiv. of zinc powder exhibits an asymmetric structure (***asym*-BCE**[5]) with dihedral angles measuring 47.74°, 45.95°, 37.31°, and 51.68° between the plane of phenyl ring and C = C bond, respectively. However, the crystal of the

https://doi.org/10.1038/s41467-024-51607-z

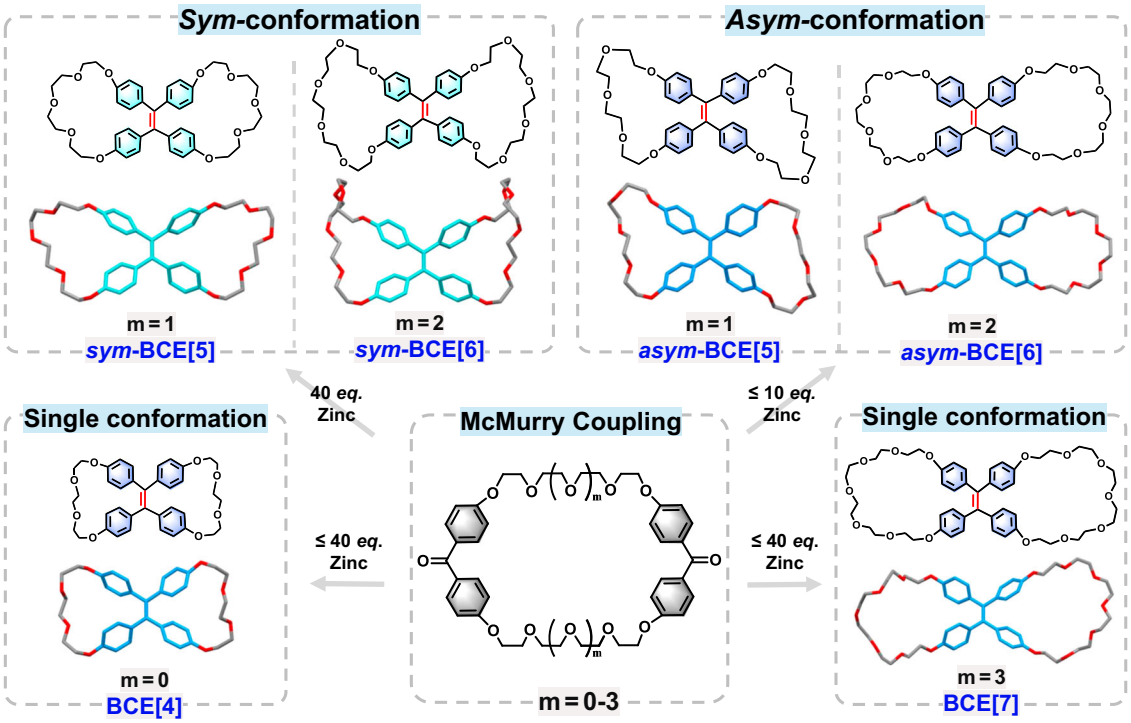

Fig. 2 | Synthesis of BCE[n]. Design strategy, synthesis routes, and different conformations of **BCE[n]** (n = 4–7).

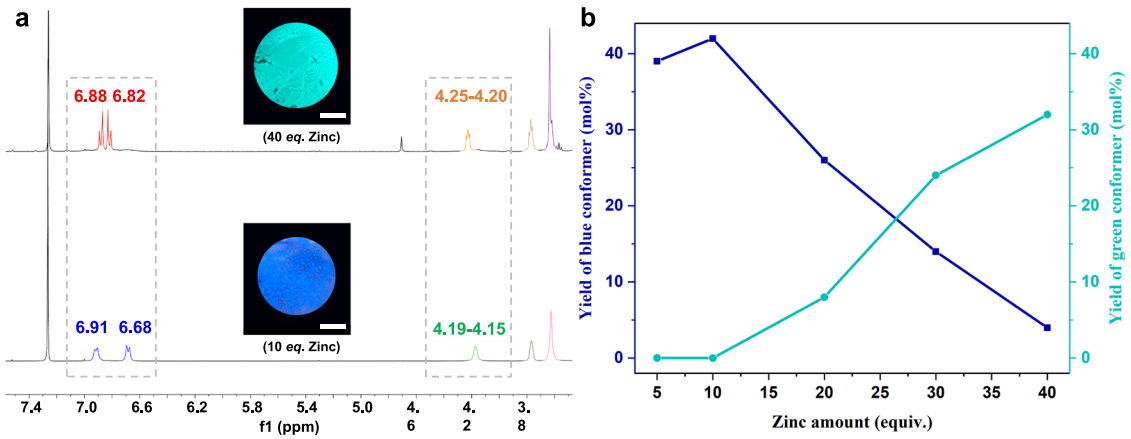

Fig. 3 | Structural characterization of two conformers. a Comparison of the ^{1}H NMR (400 MHz, $CDCl_3$, 298 K) spectra of two products (top: 40 *eq.* zinc; bottom: 10 *eq.* zinc; inset: fluorescence images excited by UV-365 nm, scale bar: 1 cm). **b** yields of two products (blue conformer and green conformer) under varying zinc amounts (5–40 *eq.* zinc).

other product obtained with 40 equiv. of zinc powder adopts a highly symmetric butterfly-shaped conformation (***sym*-BCE**[5]), with their dihedral angles measuring 54.53°, 54.53°, 44.08°, and 44.08°, respectively. Those two conformations arise from different degrees of distortion induced by flexible crown ether ring units on the phenyl rings. Both left-handed helical (*M*) conformation and right-handed (*P*) conformations can be equally observed within one unit cell, indicating that these two crystals are racemic.

The combination of NMR and single crystal data reveals that **BCE**[5] adopts two stable conformations in both solid state and solution. The crystal structures of these conformers suggest the presence of potential weak intramolecular interactions, which are likely crucial for maintaining the conformational state within this confined environment. The existence of multiple intramolecular interactions, such as C-H···O and C-H···π interactions, within the **BCE**[5] skeleton may influence both cavity shape and TPE angle. For example, due to the spatial proximity (Fig. 4a, b), ***asym*-BCE**[5] is expected to have a higher number of C-H···O interactions compared to ***sym*-BCE**[5]. Moreover, there are notable disparities in their respective stacking configurations. As shown in Fig. 4c, the crystal packing structure of symmetrical ***sym*-BCE**[5] reveals intermolecular interactions within the three adjacent molecules through C-H···O bond. In contrast, asymmetrical ***asym*-BCE**[5] displays intermolecular interactions involving four neighboring molecules, leading to a more tightly packed arrangement (Fig. 4d). This close packing restricts the rotation of TPE in the crystalline phase. Consequently, ***sym*-BCE**[5] exhibits a more obvious cyan color compared to its asymmetric counterpart (Supplementary Fig. 49).

To further investigate the disparities in molecular conformations and structures between ***sym*-BCE**[5] and ***asym*-BCE**[5], density functional theory (DFT) calculations were performed based on their respective crystal structures with Gaussian 09 software package (Revision D. 01) using M06-2X functional with 6–311 G(d, p) basis[25].

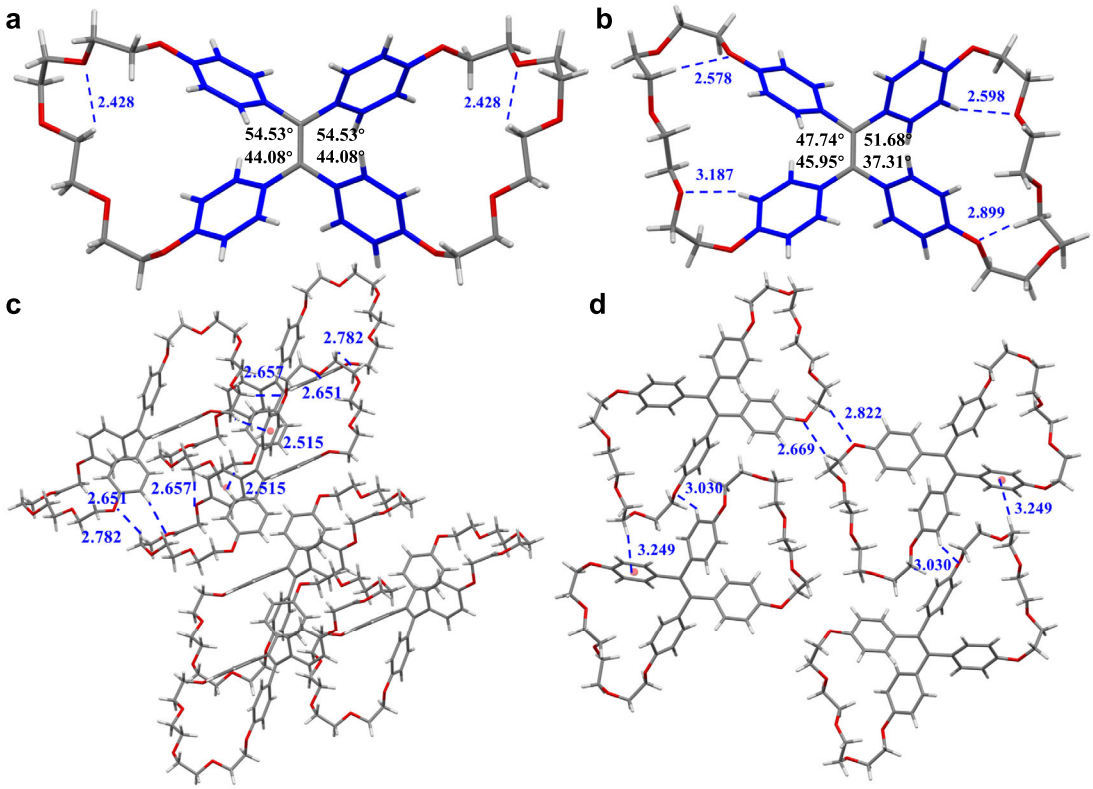

Fig. 4 | Single-crystal X-ray structure analysis of BCE[5]. Crystal structures and C − H···O distances (Å) of (**a**) ***sym*-BCE**[5] and **c** its packing mode. **b** ***asym*-BCE**[5] and **d** its packing mode. (Oxygen atoms, red; TPE, blue; Carbon atoms, gray; Hydrogen atoms, white; disordered solvent molecules are omitted for clarity).

Computationally optimized geometries confirm that both conformations resemble their original crystal structures, indicating their thermodynamic stability. The twisted conformation of ***asym*-BCE**[5] exhibits a lower energy state compared to the ***sym*-BCE**[5] conformer ($E_{asym} = -1494777.3$ kcal mol^{-1} *vs* $E_{sym} = -1494784.7$ kcal mol^{-1} according to the DFT calculation), suggesting its enhanced stability (Supplementary Fig. 50). Consequently, the structure of ***asym*-BCE**[5] is more thermodynamically stable than that of ***sym*-BCE**[5].

Based on the aforementioned experimental data and analysis, it is evident that the yields of these two conformers are influenced by the McMurry reaction condition[26–29]. The varying amounts of zinc powder may induce a templated effect, leading to a preference for one conformer in the product. Additionally, the polar surface of low-valent titanium would serve as an additional template, simultaneously promoting the formation of one stable conformer structure[30–33]. Despite the seemingly excessive amount of 10 equiv. zinc powder, the limited solubility of zinc powder in THF results in an insufficient concentration of Zn^{2+}. Consequently, this inadequate Zn^{2+} concentration within the reaction mixture leads to formation of a more stable asymmetrical conformation of ***asym*-BCE**[5] as typically observed in McMurry reactions[34]. To confirm the significance of Zn^{2+} amount on ***sym*-BCE**[5]/***asym*-BCE**[5] selectivity, we added additional $ZnCl_2$ to the previously mentioned reaction system with initially insufficient Zn^{2+}. As a result, the yield of ***sym*-BCE**[5] increased to 62.5%. To confirm the binding ability of diketone **2** with Zn^{2+}, ^{1}H NMR titration experiments were conducted, which revealed its exceptional capability in accommodating Zn^{2+} ions by electron-rich cavity (Supplementary Fig. 52). Additionally, Job's plot experiments demonstrated a 1:1 stoichiometry between diketone **2** and Zn^{2+}, indicating the formation of complexes (Supplementary Fig. 53). Based on these findings, we propose that during reagent preparation, a sufficient amount of pre-organized Zn^{2+} ions could be accommodated within the electron-rich cavity of ether rings in diketone, leading to the adoption of a specific symmetrical conformation (Supplementary Fig. 54).

To further validate the role of potential weak interactions in maintaining distinct conformations, CD_3OD was introduced into the $CDCl_3$ solution of ***sym*-BCE**[5] to investigate its ability to attenuate their intramolecular interactions (Fig. 5a). An increase in H_a' and H_b' protons and a gradual disappearance of H_a and H_b protons were observed, providing evidences for the successful transformation from ***sym*-BCE**[5] to ***asym*-BCE**[5]. In contrast, when CD_3OD was added to the $CDCl_3$ solution of ***asym*-BCE**[5], no significant change in chemical shift occurred (only solvent-induced chemical shift changes were observed). Furthermore, the influence of base/acid on the transformation from ***sym*-BCE**[5] to ***asym*-BCE**[5] was further investigated. In the case of triethylamine (TEA), which is unable to disrupt the multiple weak interactions within ***sym*-BCE**[5], no significant change in ^{1}H NMR spectra was observed upon TEA addition (Supplementary Figs. 55, 56). However, trifluoroacetic acid (TFA) can form hydrogen bonding with the ethylene glycol chain of ***sym*-BCE**[5], effectively disrupting weak interactions. The distinct chemical shifts observed within the aromatic region indicate successful conformational changes induced by TFA (Fig. 5b and Supplementary Figs. 57, 58).

In addition, variable-temperature (VT) ^{1}H NMR experiments were conducted to investigate the stability and dynamic transformation process of **BCE**[5]. To avoid the potential disruption of weak intramolecular interactions, $CDCl_3$ was chosen as the solvent. No merging or splitting phenomena were observed in the NMR spectra for any protons, indicating that increasing the solution temperature would not disrupt the intramolecular interaction and thus the conformation of ***sym*-BCE**[5] or ***asym*-BCE**[5] could be maintained (Supplementary Figs. 59, 60). Moreover, VT-NMR experiments were conducted in the solution of $C_2Br_2D_4$ (1,2-dibromoethane-1,1,2,2-d_4) to investigate its behavior at elevated temperatures (Supplementary Figs. 61, 62). The

https://doi.org/10.1038/s41467-024-51607-z

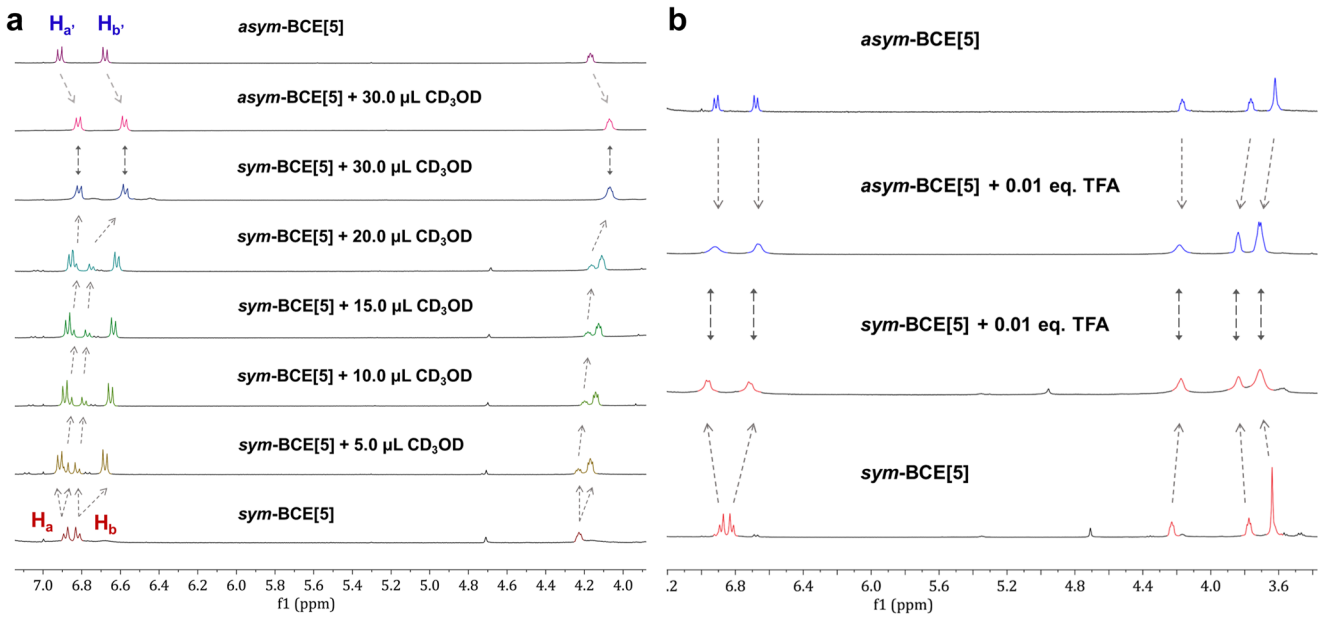

Fig. 5 | Isomerization studies on the BCE[5]. a ^{1}H NMR (400 MHz, 298 K) spectra of ***sym*-BCE**[5] (3.0 mM) in the mixed solvent (500 μL $CDCl_3$ and different contents of CD_3OD) and ***asym*-BCE**[5] in the mixed solvent (500 μL $CDCl_3$ and 30 μL CD_3OD). **b** comparison of the ^{1}H NMR (400 MHz, $CDCl_3$, 298 K) spectra of ***sym*-BCE**[5] and ***asym*-BCE**[5] (3.0 mM) with addition of 0.01 eq. TFA (blue peaks are ***asym*-BCE**[5], red peaks are ***sym*-BCE**[5]).

results indicate a subtle shift in chemical resonance, suggesting a transition from ***sym*-BCE**[5] to ***asym*-BCE**[5] (Supplementary Fig. 61), with the latter being thermodynamically more stable.

Subsequently, two conformers of TPE-embeded bis-crown ethers **BCE**[6] with longer pentaethylene glycol linkers, namely ***sym*-BCE**[6] and ***asym*-BCE**[6], were successfully synthesized (Supplementary Figs. 21–26, 41). However, it should be noted that the yield of ***sym*-BCE**[6] is significantly lower. The crystal structure of ***asym*-BCE**[6] was also obtained, as shown in Supplementary Fig. 46, similar to ***asym*-BCE**[5], the dihedral angles between the plane of phenyl ring and C = C bond were measured to be 48.96°, 40.56°, 47.83°, and 46.50°, respectively. However, our attempts to obtain the crystal structure of ***sym*-BCE**[6] were unsuccessful, so we employed DFT calculation to model its structure (Supplementary Fig. 51). The results showed that the dihedral angles of TPE in ***sym*-BCE**[6] were 46.52°, 46.52°, 48.05°, and 48.05°, respectively. Interestingly, the presence of multiple intramolecular interactions results in the formation of a small pocket within the side chain, leading to a distinct conformation of ***sym*-BCE**[6] compared to ***asym*-BCE**[6] (Fig. 6a, b). The size of the ***asym*-BCE**[6] cavity is restricted by this pocket, potentially hindering its binding with ions. The different conformations arise from varying degrees of dihedral angles of TPE induced by flexible crown ether ring units on phenyl rings. Furthermore, we successfully obtained a cocrystal of ***asym*-BCE**[6] and K^+ ion through slow vapor diffusion of *n*-hexane into acetone solution. Figure 6c illustrates that ***asym*-BCE**[6] can bind with K^+ ion in a 1:1 ratio, while another cavity is occupied by a water molecule (Supplementary Fig. 48). This indicates that the binding process between a K^+ ion and one cavity may result in reduced electron density within the adjacent cavity, thereby impeding its ability to bind another K^+ ion.

In order to further investigate the effect of glycol-linked chain length on the conformation of bis-crown ethers, we synthesized **BCE**[4] with shorter triethylene glycol side chains and **BCE**[7] with longer hexaethylene glycol side chains (Supplementary Figs. 28–33). Interestingly, only one conformer was formed in each case (Supplementary Figs. 39, 42). This can be attributed to the fact that the short rigid side chain fixes the conformation in a twisted structure, while the long flexible side chain fails to restrict the dihedral angles of TPE core, resulting in an inability to fix the conformation into specific structures. To confirm their conformations, single crystals of **BCE**[4] and **BCE**[7] were obtained through slow vapor diffusion of *n*-hexane into chloroform solution containing the macrocycles (Supplementary Figs. 43, 47). The crystal data strongly indicate that **BCE**[4] and **BCE**[7] exhibit a single conformation (the dihedral angles of TPE core in **BCE**[4] and **BCE**[7] is 37.90°, 51.35°, 47.99°, 44.00° and 42.47°, 45.84°, 50.55°, 48.46°, respectively). By integrating all experiment data, it can be deduced that the occurrence of different conformers also relies on the level of flexibility within the crown ether skeleton. This distinctive phenomenon can only be observed in the semi-rigid macrocycles **BCE**[5] and **BCE**[6].

Furthermore, the photophysical properties of the macrocycle isomers were investigated. Taking **BCE**[5] as an example, the ***sym*-BCE**[5] and ***asym*-BCE**[5] conformers both exhibited a comparable absorption profile, characterized by two distinct bands in the range of 230–430 nm (Supplementary Fig. 63). Given that **BCE**[5] possesses typical aggregation-induced emission (AIE) characteristics, we examined the AIE effect of ***sym*-BCE**[5] and ***asym*-BCE**[5] using fluorescence emission spectroscopy in chloroform-acetone mixtures with varying acetone fractions, respectively. The fluorescence intensity of ***sym*-BCE**[5] in pure chloroform initially shows a detectable response, which gradually increases upon the addition of acetone as a poor solvent, accompanied by bluish-green emission. The maximum fluorescence intensity is achieved at 455 nm when the acetone fraction reaches 90%, indicating that ***sym*-BCE**[5] exhibits typical AIE characteristics (Fig. 7a, c). Further increasing the volume fraction of acetone to 95% leads to a slight decrease in fluorescent intensity due to precipitate formation. For ***asym*-BCE**[5], it shows no significant fluorescence emission when the acetone content ranges from 0 to 90%. However, when the acetone fraction reaches 95%, it exhibits intense emission as well (Fig. 7b). In comparison to ***sym*-BCE**[5], the fluorescence emission enhancement and intensity of ***asym*-BCE**[5] were relatively low under identical conditions. It is noteworthy that the maximum emission wavelength of ***asym*-BCE**[5] at 430 nm is blue-shifted compared to that of ***sym*-BCE**[5]. This spectral shift can be attributed to their distinct packing arrangements[35,36]. What's more, the AIE behaviors of **BCE**[4] and **BCE**[7] were investigated in a mixed solvent of $CHCl_3$-*n*-hexane,

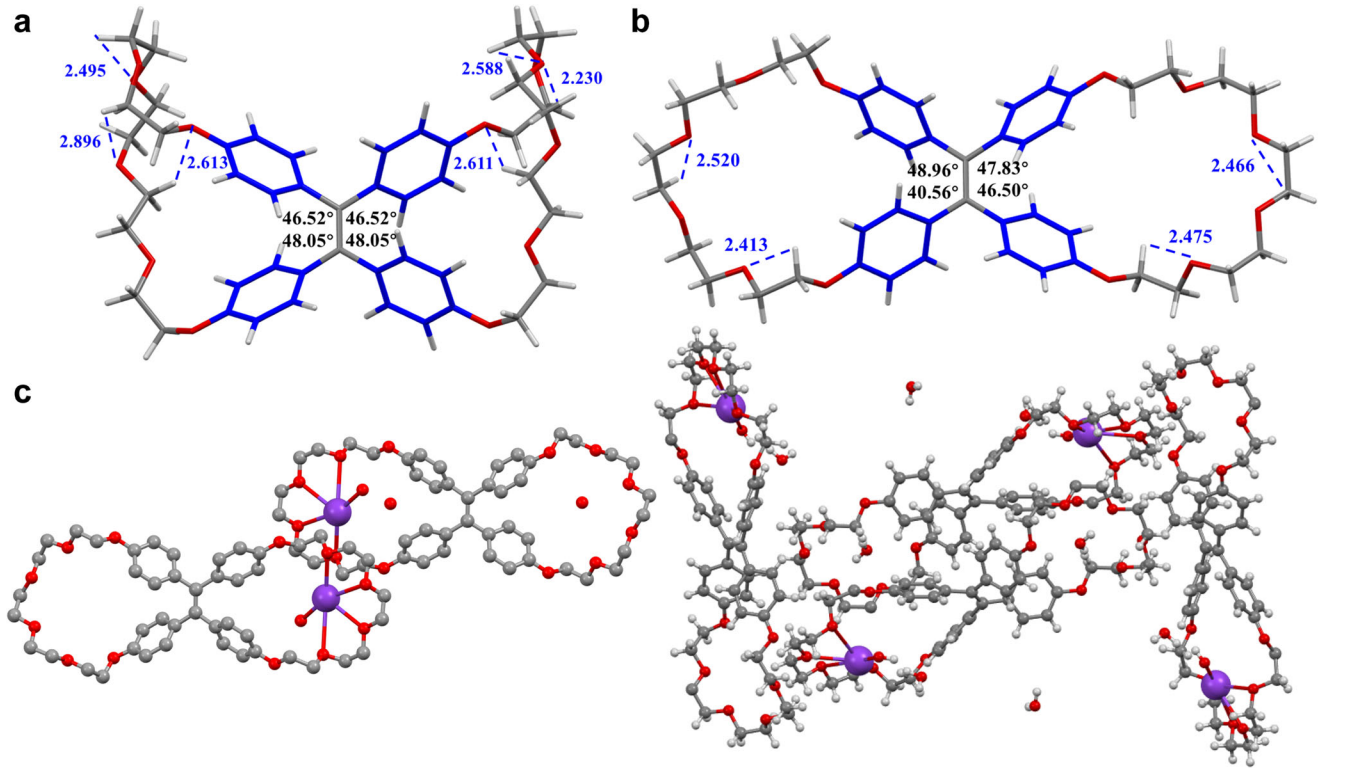

Fig. 6 | Single-crystal X-ray structure analysis of BCE[6]. **a** DFT-optimized structure for ***sym*-BCE**[6] was calculated with Gaussian 09 software package (Revision D. 01) using M06-2X functional with 6−311 G(d, p) basis. **b** crystal structure of ***asym*-BCE**[6]. **c** cocrystal of ***asym*-BCE**[6]-K^+ (OH^-, Hydrogens are omitted for clarity) and its packing mode. (Oxygen atoms, red; TPE, blue; Carbon atoms, gray; Hydrogen atoms, white; K^+ atoms, purple; disordered solvent molecules are omitted for clarity).

respectively (Supplementary Fig. 64). Compared with **BCE**[7], **BCE**[4] exhibits higher intensity and a hypsochromic shift, indicating that the shortest linker in **BCE**[4] could more efficiently restrict its rotation than the longer flexible linker in **BCE**[7]. Additionally, we also determined the absolute fluorescence quantum yield and fluorescence emission spectra of each **BCE[n]** compound in the solid states (Supplementary Figs. 65, 66). The fluorescence quantum yields were found to be 27.92% (***sym*-BCE**[5]), 25.67% (***asym*-BCE**[5]), 24.86% (***sym*-BCE**[6]), 23.36% (***asym*-BCE**[6]), 40.21% (**BCE**[4]), and 21.36% (**BCE**[7]) for different compounds, respectively. This could be attributed to the decrease in phenyl rotation restriction with longer flexible chains and different packing models.

Host-guest chemistry

The inherent helical chirality of TPE is widely recognized when the rotation of the phenyl rings is constrained[37]. Inspired by the chirality amplification phenomenon observed in supramolecular systems, we aim to induce and amplify the chirality of our macrocycles through host-guest interactions by utilizing a chiral guest molecule[38–42]. Additionally, revealing the chirality of amino acid-containing copolymers poses significant challenges due to the absence of chromophoric groups and a racemic mixture of amino acid enantiomers[43]. To address these issues, we propose an approach to design a predominant single-handed conformation between chiral amino acid co-polymer guest and **BCE[n]**, with the anticipation that the intrinsic chirality of **BCE[n]** can be induced in the presence of an additional chiral guest.

Subsequently, we constructed a supramolecular assembly through host-guest interactions between achiral **BCE[n]** and a chiral amino acid polymer $\mathbf{L_G}$ ($\mathbf{D_G}$). The structures and detailed synthesis procedures of chiral polymers $\mathbf{L_G}$ ($\mathbf{D_G}$) are provided in the Supplementary Information (Supplementary Figs. 34–38). Prior to investigating the chiral amplification between the host and the guest, we initially examined their host-guest interaction by employing benzyl *N*-benzoyl-L-alaninate ($\mathbf{G_m}$) as a model guest monomer. The complexations between each **BCE[n]** compound and $\mathbf{G_m}$ were investigated using ^{1}H NMR titration experiments. However, except for ***sym*-BCE**[5], none of the proton signals showed a significant shift when mixed with $\mathbf{G_m}$ for the other five bis-crown ethers, indicating no complexation occurred (Supplementary Figs. 70–74). As depicted in Fig. 8 and Supplementary Fig. 67, the ***sym*-BCE**[5] host experienced significant chemical shifts of the protons with increasing equivalents of $\mathbf{G_m}$. The peak of H_a, H_b, H_c, and $H_{e,f}$ in ***sym*-BCE**[5] exhibited splitting and upfield shifts. A slight upfield shift was also observed in the chemical shift of proton H_1 in $\mathbf{G_m}$. When the amount of $\mathbf{G_m}$ reached 1.0 equiv. or more, no significant changes were observed in NMR spectra, indicating a saturated condition. These observations suggest that the monomer guest $\mathbf{G_m}$ can form a stable 1:1 complex with ***sym*-BCE**[5], and the complexation between $\mathbf{G_m}$ and ***sym*-BCE**[5] exhibits a slow exchange process. Furthermore, Job's Plot analysis further verifies the binding ratio is 1:1, which may be attributed to steric hindrance limiting the binding ability of ***sym*-BCE**[5] towards a second guest (Supplementary Fig. 68). The association constant (K_a) for the ***sym*-BCE**[5]⊃$\mathbf{G_m}$ complex was determined to be 9.3×10^2 M^{-1} by UV-vis titration experiments (Supplementary Fig. 69).

Chiral amplification and regulation

Due to the induced chiral amplification from the chiral polymer guest $\mathbf{L_G}$ ($\mathbf{D_G}$) to the AIE-active host ***sym*-BCE**[5], we inferred that this supramolecular assembly could exhibit circular dichroism (CD) properties (Fig. 9a). Therefore, CD spectra were carefully examined at varying molar ratios of ***sym*-BCE**[5]/$\mathbf{L_G}$ ranging from 1:0 to 1:1.1. Upon addition of $\mathbf{L_G}$ to the achiral ***sym*-BCE**[5] solution, a strong negative cotton effect at 350 nm could be observed in the CD spectra. This can be attributed to chiral amplification of the macrocycle ***sym*-BCE**[5]

https://doi.org/10.1038/s41467-024-51607-z

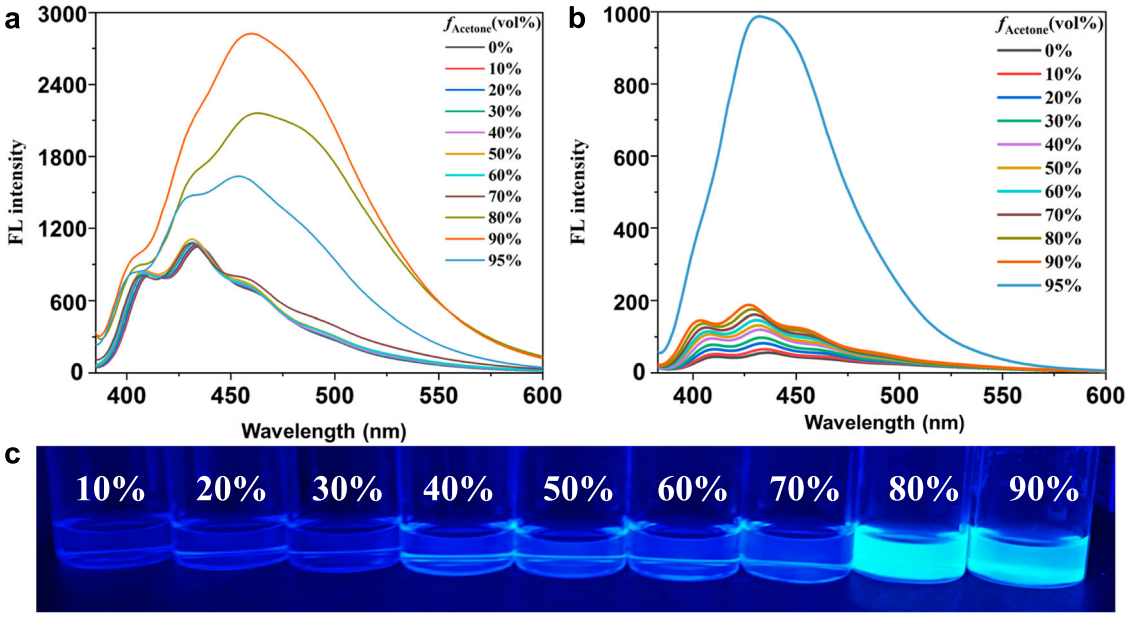

Fig. 7 | AIE properties of BCE[5]. Fluorescence spectra of **a** ***sym*-BCE**[5] and **b** ***asym*-BCE**[5] in $CHCl_3$-acetone mixed solvent with different volume fractions of acetone (λ_{ex} = 350 nm, c = 20.0 μM). **c** emission photos of ***sym*-BCE**[5] in $CHCl_3$ with $f_{acetone}$ = 10–90 vol% under 365 nm UV-light.

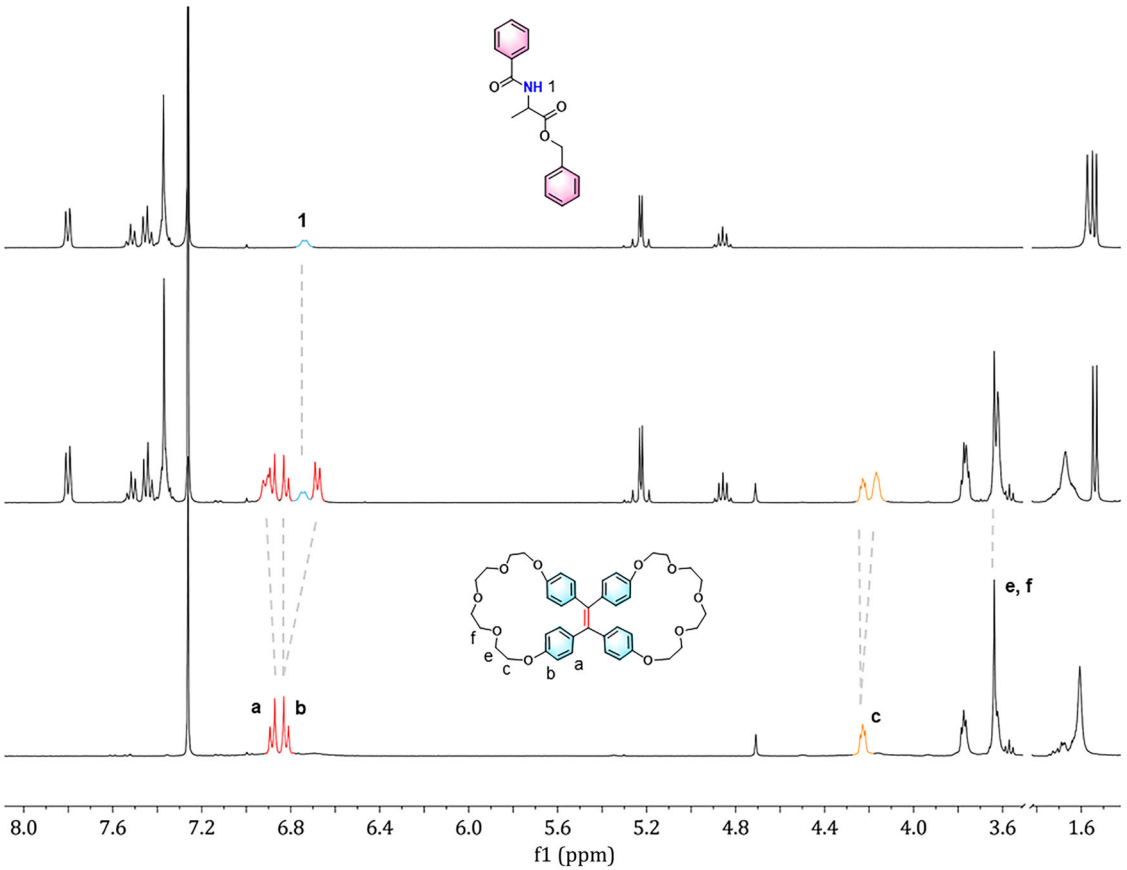

Fig. 8 | Study of host–guest interactions. ^{1}H NMR titration (400 MHz, $CDCl_3$, 298 K) spectra of ***sym*-BCE**[5] (3.0 mM), ***sym*-BCE**[5] + $\mathbf{G_m}$ (1:1, 3.0 mM) and $\mathbf{G_m}$ (3.0 mM).

induced by host-guest complexation. The highest CD intensity is achieved when $\mathbf{L_G}$ is present in an equimolar ratio with ***sym*-BCE**[5]. Further increasing $\mathbf{L_G}$ up to 1.1 equiv. did not result in significant changes in the intensity of CD signals. Therefore, our focus primarily lies on investigating the optimal stoichiometric ratio of 1:1 for achieving chiral amplification in the ***sym*-BCE**[5]⊃$\mathbf{L_G}$ system. Under identical conditions, $\mathbf{D_G}$ exhibited a positive cotton effect at 350 nm, representing mirror image CD signals compared to those obtained for the ***sym*-BCE**[5]⊃$\mathbf{L_G}$ system.

The circularly polarized luminescence (CPL) properties of the host-guest assemblies between ***sym*-BCE**[5] and chiral guest were also explored. As shown in Fig. 9b, both ***sym*-BCE**[5]⊃$\mathbf{L_G}$ and

https://doi.org/10.1038/s41467-024-51607-z

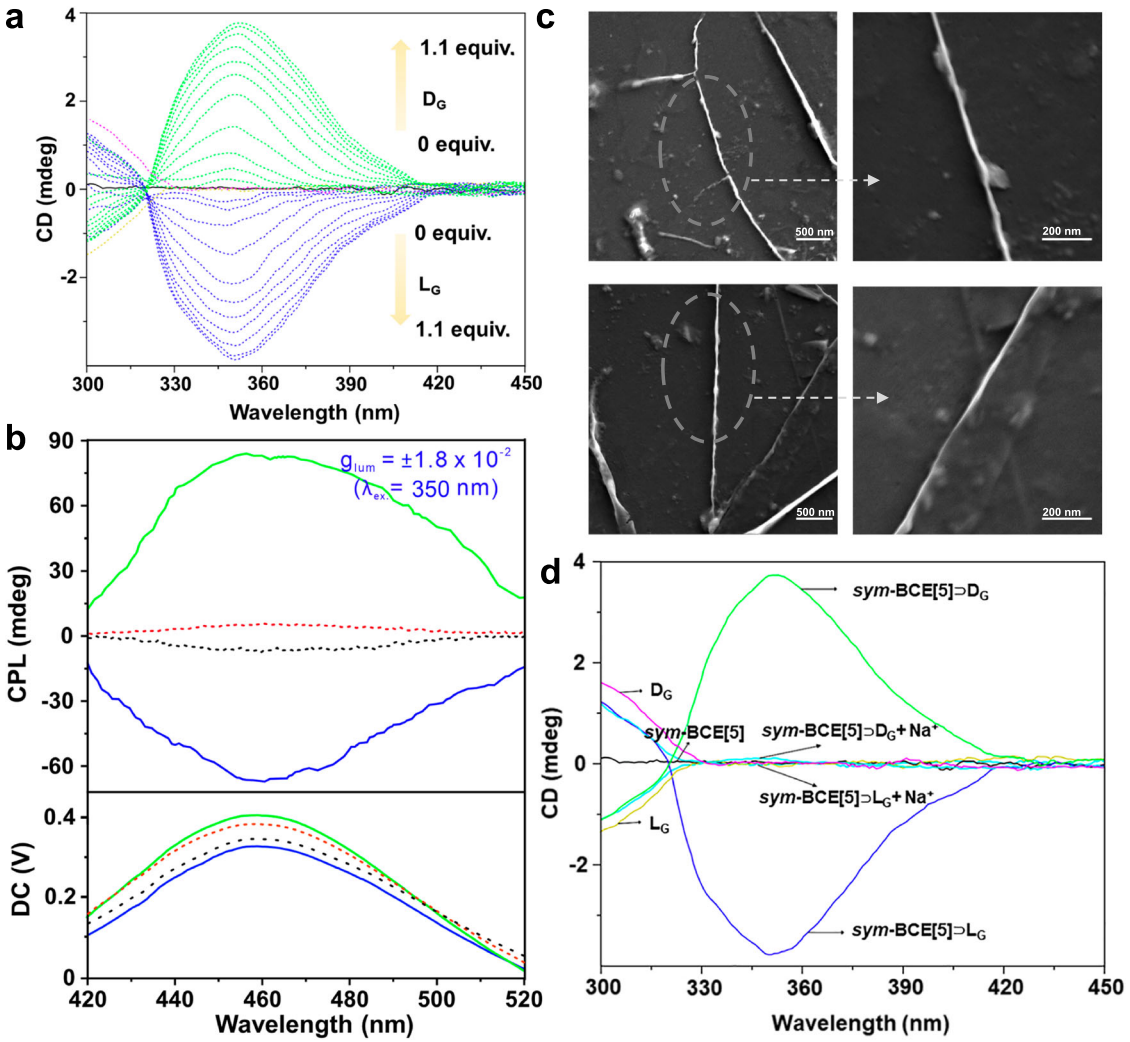

Fig. 9 | Chiral properties and micromorphology. a CD spectra of ***sym*-BCE**[5] with increasing concentrations of $\mathbf{L_G}$ and $\mathbf{D_G}$ (0 to 1.1 equiv). **b** CPL spectra of ***sym*-BCE**[5]⊃$\mathbf{L_G}$ (1:1) and $\mathbf{L_G}$ (blue and black lines, $\lambda_{ex.}$ = 350 nm), ***sym*-BCE**[5]⊃$\mathbf{D_G}$ (1:1) and $\mathbf{D_G}$ (green and red lines, λ_{ex} = 350 nm). **c** SEM images of ***sym*-BCE**[5]⊃$\mathbf{D_G}$ (up) and ***sym*-BCE**[5]⊃$\mathbf{L_G}$ (bottom). **d** CD spectra of $\mathbf{L_G}$, $\mathbf{D_G}$, ***sym*-BCE**[5]⊃$\mathbf{L_G}$ (1:1), ***sym*-BCE**[5]⊃$\mathbf{D_G}$ (1:1), ***sym*-BCE**[5]⊃$\mathbf{L_G}$ + Na^+ (1:1:1) and ***sym*-BCE**[5]⊃$\mathbf{D_G}$ + Na^+ (1:1:1).

***sym*-BCE**[5]⊃$\mathbf{D_G}$ complexes exhibited a pair of mirror-image CPL signals in the range of 400–500 nm due to the chiral amplification facilitated by strong host-guest interactions and well-order assembled nanostructures. The maximum g_{lum} values of CPL for ***sym*-BCE**[5]⊃$\mathbf{L_G}$ and ***sym*-BCE**[5]⊃$\mathbf{D_G}$ were determined to be -1.80×10^{-2} and 1.84×10^{-2} at 455 nm, respectively. In contrast, the guest $\mathbf{L_G}$ and $\mathbf{D_G}$ alone did not exhibit any CPL signals at any wavelength, highlighting the essential role played by the AIE-active achiral host in facilitating optical performance.

Subsequently, transmission electron microscopic (TEM) and scanning electron microscopy (SEM) measurements were utilized to explore the morphologies of polymeric guests and their assemblies. TEM images revealed that $\mathbf{L_G}$ or $\mathbf{D_G}$ self-assembled into nanowire structure with average widths of ~100 nm and 200 nm in chloroform, respectively (Supplementary Fig. 81). When ***sym*-BCE**[5] was mixed with $\mathbf{L_G}$, SEM and TEM images clearly showed that the resulting supramolecular complex ***sym*-BCE**[5]⊃$\mathbf{L_G}$ exhibited a left-handed linear nanostructure with helixes, while $\mathbf{D_G}$ with the opposite molecular chirality formed a right-handed nano-helical structure (Fig. 9c, and Supplementary Fig. 81).

Based on the aforementioned investigation of host-guest interactions, ***sym*-BCE**[5] exhibited superior binding properties towards guest molecules, making it an ideal candidate for further comprehensive exploration. Considering the potential site for metal ion binding with crown ether rings, the introduction of competitive metal ions could effectively regulate the chiral assemblies. It is widely recognized that sodium cations exhibit a stronger affinity towards crown ethers compared to secondary amines[44–49]. Therefore, sodium tetrakis[3,5-bis(trifluoromethyl)-phenyl]borate (NaBArF) was selected as a competitive guest to modulate the CD and CPL switching behavior of the host-guest complex, presenting an innovative approach for fabricating dynamic CPL-active materials[50].

The binding behavior of Na^+ cation to ***sym*-BCE**[5] was investigated using ^{1}H NMR spectroscopy in $CDCl_3$ solution. Upon addition of Na^+, significant chemical shift changes were observed, with the maximum chemical shift reached when one equivalent of Na^+ was added (Supplementary Fig. 75). This observation suggests the formation of a 1:1 complex between ***sym*-BCE**[5] and Na^+. Furthermore, the binding behavior exhibited fast exchange kinetics on the NMR spectroscopic timescale. Job's Plot confirmed a 1:1 stoichiometry similar to **BCE**[6] in its binding with K^+ ion (Supplementary Fig. 76), and the association constant (K_a) was calculated as 2.70×10^3 M^{-1} by analyzing sequential changes in UV-vis absorbance of ***sym*-BCE**[5] in the presence of varying concentrations of Na^+ (Supplementary Fig. 77). This indicates that Na^+ competes effectively in regulating the self-assembly of ***sym*-BCE**[5]-based assemblies. In contrast, minimal changes in chemical shifts were

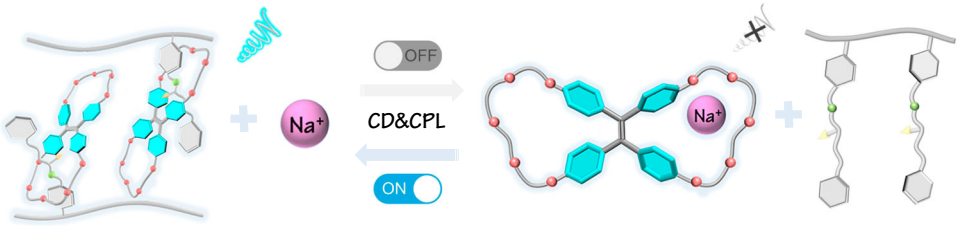

Fig. 10 | The mechanism for tunable chiral polymer. Cartoon representation of the CD and CPL signal of ***sym*-BCE**[5]⊃$\mathbf{L_G}$ ($\mathbf{D_G}$) can be modulated by Na^+.

observed in the $CDCl_3$ solution of ***asym*-BCE**[5] under identical conditions, suggesting a lack of strong binding affinity between ***asym*-BCE**[5] and Na^+ cation (Supplementary Fig. 78). This could be attributed to the unfavorable effect of its more twisted and smaller-sized cavities on guest binding of ***asym*-BCE**[5].

Titration experiments were further conducted to investigate the CD spectra changes upon adding Na^+ cations (0 to 1.0 eq.), aiming to induce the CD/CPL switching process. As a result, CD spectra exhibited a quenching effect on the CD signal with increasing amounts of Na^+ (Supplementary Fig. 80). Consequently, as shown in Fig. 9d, the addition of Na^+ resulted in a decrease in CD intensity for both ***sym*-BCE**[5]⊃$\mathbf{L_G}$ and ***sym*-BCE**[5]⊃$\mathbf{D_G}$, indicating disassembly of assemblies. Based on these observations, it can be inferred that competitive binding of Na^+ to the ***sym*-BCE**[5] host leads to a simultaneous switch-off in both CD and CPL signals for the supramolecular assemblies (Fig. 10).

Discussion

In conclusion, a series of bis-crown ether named **BCE[n]** ($n = 4–7$) with AIE-active TPE cores were synthesized by intramolecular coupling of cyclic precursor diketone compounds. The incorporation of flexible side chains into the rigid TPE core resulted in a specific strain on the molecules, leading to the existence of two conformers in semi-rigid **BCE**[5] and **BCE**[6], depending on the chain length. These conformers exhibit varying dihedral angles within the TPE core and variations in the shapes of crown ether cavities. Additionally, they can be effectively purified using conventional column chromatography. Due to subtle differences in conformation and ring size, their unique host-guest selective binding behaviors as well as their photophysical properties were systematically investigated. By utilizing host-guest interaction and supramolecular chiral amplification, ***sym*-BCE**[5]-based chiral assemblies were constructed to demonstrate both CD and CPL signals in the presence of chiral polymeric guests. Furthermore, these assemblies also exhibit Na^+-responsive switch-off for CD and CPL signals. This highlights the significance of conformational diversification in elucidating the exceptional properties of supramolecular macrocycles while providing valuable insights into their structure-property relationships.

Methods

General procedures for the synthesis of diketone derivatives

Under an argon atmosphere, a mixture of 4,4′-dihydroxybenzophenone (1.0 mmol), compound glycol ditosylate (2.5 mmol), KI (0.25 mmol), and K_2CO_3 (20.0 mmol) in anhydrous MeCN (10 mL) was refulxed overnight. The reaction mixture was filtered and rinsed three times with DCM. Organic layer was washed with deionized water, dried over Na_2SO_4. After filtration, the organic layer was collected and concentrated under vacuum. The crude product was purified by column chromatography over silica gel (ethyl acetate/petroleum ether, 1:1, *v/v*) to afford dieketone derivatives **1**–**4** as a white soild.

General procedures for the systhesis of *asym*-BCE[n] ($n = 5, 6$). Under nitrogen atmosphere, diketone derivative (1.0 mmol) and zinc powder (10.0 mmol) were dissolved in anhydrous THF (10 mL). The mixture was cooled to −10 °C and $TiCl_4$ (5.0 mmol) was slowly added. After stirring for 1 h, the reaction mixture was warmed to room temperature and then refluxed overnight. The reaction was quenched by the addition of $NaHCO_3$ solution. After filtration, the organic layer was collected and concentrated. The crude product was purified by silica gel column chromatography using PE/EA = 2/1, *v/v*) as eluent to obtain a colorless soild ***asym*-BCE[n]**.

General procedures for the synthesis of *sym*-BCE[n] ($n = 5, 6$). Under nitrogen atmosphere, diketone derivative (1.0 mmol) and zinc powder (40.0 mmol) were dissolved in anhydrous THF (10 mL). The mixture was cooled to −10 °C and $TiCl_4$ (20.0 mmol) was slowly added. After stirring for 1 h, the reaction mixture was warmed to room temperature and then refluxed overnight. The reaction was quenched by the addition of $NaHCO_3$ solution. After filtration, the organic layer was collected and concentrated. The crude product was purified by silica gel column chromatography using PE/EA = 2/1, *v/v*) as eluent to obtain a colorless soild ***sym*-BCE[n]** as a major product and ***asym*-BCE[n]** as a minor product.

Preparation of BCE[n]

The synthesis and characterization of **BCE[n]** ($n = 4–7$) presented in this work, the experimental details, and additional data of tests were listed in the Supplementary Information.

Characterization methods

NMR spectra were recorded on a Bruker AV400 and AV600 (400 MHz and 600 MHz) spectrometer. High-resolution electrospray ionization mass spectra (HR-ESI-MS) were recorded on an Agilent 6540Q-TOF LCMS equipped with an electrospray ionization (ESI) probe operating in the positive-ion mode with direct infusion. UV-vis absorption spectra were taken on a SHIMADZU UV-1700 spectrometer. Fluorescence spectra of solutions and powder were recorded on an Edinburg FLS-1000 steady-state and time-resolved fluorescence spectrometer using a xenon lamp as the excitation source. The absolute fluorescence quantum yield in the solid state was measured by using a calibrated integrating sphere on the same fluorescence spectrometer. CD spectra were determined using a JASCO J-810 spectrometer. CPL spectra were recorded by using a JASCO CPL-300 spectrometer. TEM analysis was performed on a JEM-2100 instrument. SEM images were captured with a Hitachi S-4700 microscope. Single crystal X-ray diffraction data were collected on a Bruker D8 VENTURE CMOS X-ray diffractometer (Mo−Kα radiation, λ = 0.71073 Å).

Data availability

The X-ray crystallographic coordinates for structures reported in this study have been deposited at the Cambridge Crystallographic Data Center (CCDC), under deposition numbers 2323861 (**BCE**[4]); 2242720 (***asym*-BCE**[5]); 2323862 (***sym*-BCE**[5]); 2323863 (***asym*-BCE**[6]); 2323865 (**BCE**[7]); 2323867 (***asym*-BCE**[6] + $\mathbf{K^+}$ complexes). These data can be obtained free of charge from The Cambridge Crystallographic Data Center via www.ccdc.cam.ac.uk/data_request/cif. The authors declare that the data supporting the findings of this study are available within the paper and its Supplementary Information. And the

coordinates of computationally determined structures are available from source data. The additional data can be obtained from the corresponding author. Source data are provided in this paper.

References

1. Feng, H.-T., Yuan, Y.-X., Xiong, J.-B., Zheng, Y.-S. & Tang, B. Z. Macrocycles and cages based on tetraphenylethylene with aggregation-induced emission effect. *Chem. Soc. Rev.* **47**, 7452–7476 (2018).
2. Lou, X.-Y. & Yang, Y.-W. Manipulating aggregation-induced emission with supramolecular macrocycles. *Adv. Optical Mater.* **6**, 1800668 (2018).
3. Wang, K. et al. Dimeric pillar[5]arene as a novel fluorescent host for controllable fabrication of supramolecular assemblies and their photocatalytic applications. *Adv. Sci.* **10**, 2206897 (2023).
4. Ye, Y. et al. Self-assembly of chiral metallacycles and metallacages from a directionally adaptable BINOL-derived donor. *J. Am. Chem. Soc.* **137**, 11896–11899 (2015).
5. Dong, J. et al. Ultrathin two-dimensional porous organic nanosheets with molecular rotors for chemical sensing. *Nat. Commun.* **8**, 1142 (2017).
6. Wang, J.-H., Feng, H.-T. & Zheng, Y.-S. Synthesis of tetraphenylethylene pillar[6]arenes and the selective fast quenching of their AIE fluorescence by TNT. *Chem. Commun.* **50**, 11407–11410 (2014).
7. Feng, M., Zhang, J., Ji, H.-T., Xu, X.-D. & Feng, S. Tetraphenylethene-based macrocycles: visualized monitoring the hydrolysis of silicon-oxygen bond and their tunable luminescent properties. *Chem. Eng. J.* **463**, 142241 (2023).
8. Shultz, D. A. & Fox, M. A. Effect of phenyl ring torsional rigidity on the photophysical behavior of tetraphenylethylenes. *J. Am. Chem. Soc.* **111**, 6311–6320 (1989).
9. Shustova, N. B., Cozzolino, A. F. & Dincă, M. Conformational locking by design: relating strain energy with luminescence and stability in rigid metal–organic frameworks. *J. Am. Chem. Soc.* **134**, 19596–19599 (2012).
10. Huang, Q. et al. An exceptionally flexible hydrogen-bonded organic framework with large-scale void regulation and adaptive guest accommodation abilities. *Nat. Commun.* **10**, 3074 (2019).
11. Guo, Z. et al. Drum-like metallacages with size-dependent fluorescence: exploring the photophysics of tetraphenylethylene under locked conformations. *J. Am. Chem. Soc.* **143**, 9215–9221 (2021).
12. Han, B., Zhu, L., Wang, X., Bai, M. & Jiang, J. Conformation-controlled emission of AIE luminogen: a tetraphenylethene embedded pillar[5]arene skeleton. *Chem. Commun.* **54**, 837–840 (2018).
13. Guo, Z. et al. Conformational effect on fluorescence emission of tetraphenylethylene-based metallacycles. *Chin. Chem. Lett.* **32**, 1691–1695 (2021).
14. Liu, C., Yang, G., Si, Y. & Pan, X. Photophysical properties of chiral tetraphenylethylene derivatives with the fixed propeller-like conformation. *J. Phys. Chem. C.* **122**, 5032–5039 (2018).
15. Zhou, Z. et al. Immobilizing tetraphenylethylene into fused metallacycles: shape effects on fluorescence emission. *J. Am. Chem. Soc.* **138**, 13131–13134 (2016).
16. Xiong, J.-B. et al. Evidence for aggregation-induced emission from free rotation restriction of double bond at excited state. *Org. Lett.* **20**, 373–376 (2018).
17. Mu, C. et al. Tetraphenylethylene-based multicomponent emissive metallacages as solid-state fluorescent materials. *Angew. Chem. Int. Ed.* **60**, 12293–12297 (2021).
18. Qu, H. et al. Molecular face-rotating cube with emergent chiral and fluorescence properties. *J. Am. Chem. Soc.* **139**, 18142–18145 (2017).
19. Xiong, J.-B. et al. The fixed propeller-like conformation of tetraphenylethylene that reveals aggregation-induced emission effect, chiral recognition, and enhanced chiroptical property. *J. Am. Chem. Soc.* **138**, 11469–11472 (2016).
20. Sun, Y.-L. et al. Chiral emissive porous organic cages. *Chem. Commun.* **59**, 302–305 (2023).
21. Nian, H. et al. Tetraphenylethene-based tetracationic dicyclophanes: synthesis, mechanochromic luminescence, and photochemical reactions. *Chem. Commun.* **56**, 3195–3198 (2020).
22. Zhang, J., Kang, W. & Xu, X.-D. Tetraphenylethene-based macrocycles with dual-ring topology: synthesis, structures, and applications. *Org. Chem. Front.* **10**, 6225–6239 (2023).
23. Tanaka, Y., Machida, T., Noumi, T., Sada, K. & Kokado, K. Emissive tetraphenylethylene (TPE) derivatives in a dissolved state tightly fastened by a short oligo(ethylene glycol) chain. *Org. Chem. Front.* **7**, 2649–2656 (2020).
24. Song, S. & Zheng, Y.-S. Hollow spheres self-assembled by a tetraphenylethylene macrocycle and their transformation to bird nests under ultrasound. *Org. Lett.* **15**, 820–823 (2013).
25. Frisch, M. J. et al. Gaussian 09, Revision D.01, Gaussian, Inc., Wallingford CT (2013).
26. Gupta, S., Kar, G. K. & Ray, J. K. Stereoselective synthesis of 1,6-Dichloro-1,3,5-Hexatriene derivatives by McMurry coupling of β-chloroacrylaldehyde derivatives. *Synth. Commun.* **30**, 2393–2399 (2000).
27. Bongso, A., Roswanda, R. & Syah, Y. M. Recent advances of carbonyl olefination via McMurry coupling reaction. *RSC Adv.* **12**, 15885–15909 (2022).
28. McMurry, J. E. Carbonyl-coupling reactions using low-valent titanium. *Chem. Rev.* **89**, 1513–1524 (1989).
29. José Manuel, B.-A., María Jesús, D.-P., James, R. H., Rosario, H.-G. & Isidro, G. C. $Cp_2Ti(III)Cl$ and analogues as sustainable templates in organic synthesis. *Synthesis* **50**, 2163–2180 (2018).
30. Hoss, R. & Vogtle, F. Template syntheses. *Angew. Chem. Int. Ed.* **33**, 375–384 (1994).
31. Fürstner, A., Seidel, G., Kopiske, C., Krüger, C. & Mynott, R. Syntheses, structures, and complexation properties of photoresponsive crownophanes. *Liebigs Ann. /Recl.* **1996**, 655–662 (1996).
32. Mayekar, N. V., Chattopadhyay, S. & Nayak, S. An efficient synthetic strategy for geometrically pure symmetrical and unsymmetrical hydroxystilbenes via McMurry coupling. *Synthesis* **13**, 2041–2046 (2003).
33. Duan, X.-F., Zeng, J., Lü, J.-W. & Zhang, Z.-B. Insights into the general and efficient cross McMurry reactions between ketones. *J. Org. Chem.* **71**, 9873–9987 (2006).
34. Bogdanović, B. & Bolte, A. A comparative study of the McMurry reaction utilizing $[HTiCl(THF)_{-0.5}]_x$, $TiCl_3(DME)_{1.5}$-Zn(Cu) and $TiCl_2$·LiCl as coupling reagents. *J. Organomet. Chem.* **502**, 109–121 (1995).
35. Yao, P. et al. Insights into molecular packing effects on the emission properties of fluorenone-based molecules in the aggregate state. *J. Mater. Chem. C.* **9**, 13687–13696 (2021).
36. Lei, S.-N. et al. BowtieArene: a dual macrocycle exhibiting stimuli-responsive fluorescence. *Angew. Chem. Int. Ed.* **59**, 10059–10065 (2020).
37. Hu, M. et al. Hindered tetraphenylethylene helicates: chiral fluorophores with deep-blue emission, multiple-color CPL, and chiral recognition ability. *Angew. Chem. Int. Ed.* **61**, e202115216 (2022).
38. Ji, L. et al. Host–guest interaction enabled chiroptical photoswitching and enhanced circularly polarized luminescence. *Chem. Commun.* **55**, 11747–11750 (2019).
39. Cheng, L. et al. Adaptive chirality of an achiral cage: chirality transfer, induction, and circularly polarized luminescence through aqueous host–guest complexation. *CCS Chem.* **2**, 2749–2763 (2020).
40. Cheng, L. et al. Chiral adaptive recognition with sequence specificity of aromatic dipeptides in aqueous solution by an achiral cage. *Chem. Sci.* **14**, 833–842 (2023).

41. Li, J., Zhou, H.-Y., Han, Y. & Chen, C.-F. Saucer[n]arenes: synthesis, structure, complexation, and guest-induced circularly polarized luminescence property. *Angew. Chem. Int. Ed.* **60**, 21927–21933 (2021).
42. Quan, M., Pang, X.-Y. & Jiang, W. Circular dichroism based chirality sensing with supramolecular host–guest chemistry. *Angew. Chem. Int. Ed.* **61**, e202201258 (2022).
43. Velmurugan, K. et al. Supramolecular nanohelix fabricated by pillararene-based host–guest system for chirality amplification, transfer, and circularly polarized luminescence in water. *CCS Chem.* **4**, 3426–3439 (2022).
44. Pedersen, C. J. The discovery of crown ethers. *Science* **241**, 536–540 (1988).
45. Zheng, B., Wang, F., Dong, S. & Huang, F. Supramolecular polymers constructed by crown ether-based molecular recognition. *Chem. Soc. Rev.* **41**, 1621–1636 (2012).
46. Gokel, G. W., Matthew Leevy, W. & Weber, M. E. Crown Ethers: sensors for ions and molecular scaffolds for materials and biological models. *Chem. Rev.* **104**, 2723–2750 (2004).
47. Ruiz-Hitzky, E. & Casal, B. Crown ether intercalations with phyllosilicates. *Nature* **276**, 596–597 (1978).
48. Ren, C., Shen, J. & Zeng, H. Combinatorial evolution of fast-conducting highly selective K^+-channels via modularly tunable directional assembly of crown ethers. *J. Am. Chem. Soc.* **139**, 12338–12341 (2017).
49. Wagner, M. J., Huang, R. H., Eglin, J. L. & Dye, J. L. An electride with a large six-electron ring. *Nature* **368**, 726–729 (1994).
50. Guo, F. et al. Chiroptical switching of molecular universal joint triggered by complexation/release of a cation: a stepwise synergistic complexation. *Chin. Chem. Lett.* **34**, 107558 (2023).

Acknowledgements

This work was supported by the National Natural Science Foundation of China (Nos. 22271154 and M-0411), the Innovation Support Program of Jiangsu Province (BZ2023055), and the China Postdoctoral Science Foundation project (2022M721601). The authors thank Prof. Myongsoo Lee, Prof. Jochen Niemeyer, Prof. Leyong Wang, and Prof. Yong Liang for their valuable suggestions.

Author contributions

X. T. and M. Z. contributed equally to this work. X. T. and M. Z. drafted the manuscript and conceived the project. X.-Y. H. supervised the project and revised the manuscript. X. T., Y. S., N. M., Y. S., and K. V. performed the experiments. K. W. and J. J. helped with X-ray crystallography characterization. All authors collectively analyzed the data, discussed the results, and provided comments on the manuscript.

Competing interests

The authors declare no competing interests.

Additional information

Supplementary information The online version contains supplementary material available at https://doi.org/10.1038/s41467-024-51607-z.

Correspondence and requests for materials should be addressed to Xiao-Yu Hu.

Peer review information *Nature Communications* thanks the anonymous reviewer(s) for their contribution to the peer review of this work. A peer review file is available.